

Rapid cardiac activation prediction for cardiac resynchronization therapy planning using geometric deep learning

Ehsan Naghavi^{1,2}, Haifeng Wang¹, Vahid Ziaei Rad¹, Julius Guccione^{2,3}, Ghassan Kassab^{2,3}, Vishnu Boddeti⁴, Seungik Baek¹, and Lik-Chuan Lee^{*1}

¹Dept. of Mechanical Engineering, Michigan State University, East Lansing, MI

²3DT Holdings, LLC, San Diego, CA

³California Medical Innovations Institute, San Diego, CA

⁴Dept. of Computer Science and Engineering, Michigan State University, East Lansing, MI

Abstract

Cardiac resynchronization therapy (CRT) is a common intervention for patients with dyssynchronous heart failure, yet approximately one-third of recipients fail to respond due to suboptimal lead placement. Identifying optimal pacing sites remains challenging, largely due to patient-specific anatomical variability and the limitations of current individualized planning strategies. In a step towards constructing an *in-silico* approach to help address this issue, we develop two geometric deep learning (DL) models, based on graph neural network (GNN) and geometry-informed neural operator (GINO), to predict cardiac activation time map in real-time for CRT planning and optimization. Both models are trained on a large synthetic dataset generated from finite-element (FE) simulations over a wide range of left ventricular (LV) geometries, pacing site configurations, and tissue conductivities. The GINO model significantly outperforms the GNN model, with lower prediction errors (1.14% vs 3.14%) and superior robustness to noise and various mesh discretization. Using the GINO model, we also develop a workflow for optimizing the pacing site in CRT from given activation time map and LV geometry. Compared to randomly selecting a pacing site, the CRT optimization workflow produces a larger reduction in maximum activation time (20% vs. 8%). In conjunction with an interactive web-based graphical user interface (GUI) available at <https://dcsim.egr.msu.edu/>, the GINO model shows promising potential as a clinical decision-support tool for personalized pre-procedural CRT optimization.

Keywords: Cardiac resynchronization therapy, Geometric deep learning, Neural operators, Graph neural networks, Cardiac electrophysiology

*Corresponding author: llee@egr.msu.edu

1 Introduction

In patients with dyssynchronous heart failure, cardiac resynchronization therapy (CRT) is an established treatment to restore synchronized ventricular activation patterns [1–4]. Despite its efficacy, approximately one-third of CRT recipients do not experience optimal outcomes and are classified as non-responders [1, 5]. Contributing factors of CRT non-response include the heterogeneity of left ventricular (LV) anatomy and challenges associated with individualized lead placement strategies [6–10]. Although the importance of pacing site selection is emphasized in numerous experimental and clinical studies [10–14], its optimization in clinical practice remains difficult [15].

To address this issue, physics-based computational models based on differential equations have been developed to provide insights into CRT mechanisms and assist in therapy optimization [16–25]. While these models can provide high-fidelity predictions, their dependence on computationally expensive numerical methods limits their practical use in time-sensitive clinical scenarios. To overcome this limitation, deep learning (DL) methodologies are increasingly used to develop surrogate models capable of rapid predictions with reasonable accuracy [26–37]. DL models specifically for optimizing pacing site selection in CRT, however, remain scarce. Most machine learning studies have primarily focused on classifying treatment responses based on clinical characteristics (e.g., ischemia versus non-ischemia) [38–43], rather than modeling and optimizing the effects of various pacing sites to enhance therapeutic outcomes.

Accommodating arbitrary patient-specific heart geometries is a major challenge for developing DL surrogates. Convolutional neural network (CNN)-based methods are restricted to structured grids [44], and approaches tailored to single geometries necessitate retraining for each new patient [45, 46]. Reduced-order models [47, 48], though offering some flexibility, frequently fail to capture localized anatomical features crucial for precise predictions, thereby restricting the clinical utility of DL-based CRT planning tools.

Graph neural networks (GNNs) have emerged as a promising approach for learning simulations in irregular domains [49]. By representing geometries as graph-structured data composed of nodes and edges, GNNs naturally handle arbitrary geometries and have been applied in cardiovascular research [50–54]. Concurrently, neural operators have recently gained attention for their ability to learn mappings between infinite-dimensional function spaces, in contrast to conventional neural networks that typically map between finite-dimensional vector spaces [55]. This capability offers a principled approach to modeling solution operators of differential equations, making neural operators particularly suitable for scientific modeling tasks on continuous domains [56], such as in cardiovascular simulations. Despite their potential, neural operators have only recently been applied to cardiovascular problems [57].

Here, we develop and compare two physics-based DL models to predict cardiac activation patterns in the LV that can potentially be used for CRT planning. The first model utilizes a GNN architecture (Graph-UNet) [58], whereas the second employs geometry-informed neural operator (GINO) [59]. Both models can handle arbitrary spatial domains and fall under geometric deep learning, which embeds geometric inductive biases into DL models for enhanced performance [60]. By comparing these two models, we aim to investigate whether the neural operator framework, designed to learn mappings between function spaces, offers advantages over the GNN-based approach for this application.

Operating directly on point cloud representations of LV geometries, we show that the trained DL models can rapidly and accurately predict activation patterns across arbitrary

LV geometries, tissue conductivity, and pacing sites. To enhance user accessibility, we developed an interactive web-based graphical user interface (GUI) employing the trained DL models in the backend. We also demonstrate the clinical applicability of the DL models by developing a workflow to optimize the pacing site from a given LV geometry and an activation time map.

2 Methods

We developed physics-based DL models capable of rapidly mapping patient-specific LV geometry, pacing site(s), and tissue electrical conductivity to corresponding activation patterns. To accomplish this, we generated a large set of paired input-output data through numerical simulations. First, we created thousands of synthetic LV geometries using the methodology adapted by Buoso *et al.* [32]. These geometries were then utilized in finite-element (FE) simulations of cardiac electrophysiology to compute activation patterns associated with randomly selected pacing sites. Additionally, tissue electrical conductivity values were varied to reflect inter-subject variability (see Fig. 1). Finally, this dataset was used to train our DL models. Detailed descriptions of each step are provided in the subsequent subsections.

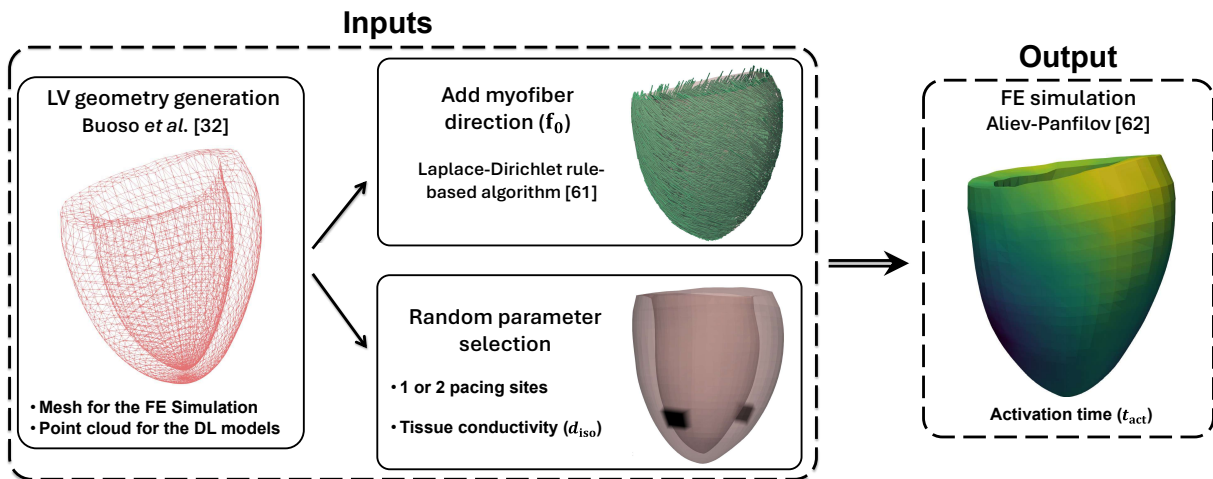


Figure 1: Generation of input-output dataset for training and testing the DL models. A synthetic LV geometry is generated using the method described by Buoso *et al.* [32]. The mesh is used for the FE simulation, whereas only the corresponding point cloud is retained for the DL models. LV myofiber direction is computed using a Laplace-Dirichlet rule-based algorithm [61]. One or two pacing sites, and a random subject specific tissue electrical conductivity value are selected. The activation pattern is computed by solving the Aliev-Panfilov model [62] using the FE method. A total of 17,500 simulations were conducted to generate the dataset used for training the DL models.

2.1 Generation of synthetic LV geometries

Synthetic geometries were generated following the methodology proposed by Buoso *et al.* [32]. Their approach utilizes proper orthogonal decomposition (POD) to create a shape model based on a dataset of 75 segmented LV geometries derived from healthy individuals and patients with cardiovascular diseases aged between 5 and 80 years. The model maps a reference LV mesh, comprising 21,240 tetrahedral elements and 4,804 nodes, to capture geometric variations of the LV within the dataset.

Each mesh was preprocessed following the original methodology and aligned to a common Cartesian coordinate frame. Specifically, the centroid of the basal endocardial contour was positioned at the origin, the normal to the basal cut-plane was aligned with the positive z -axis (base-apex direction), and the inferior intersection of the valve ring was aligned with the negative x -axis.

Here, synthetic LV geometries were generated by randomly selecting coefficients for the first four POD bases within ranges defined by the POD analysis. Fig. 2 shows geometric variations associated with each basis. A total of 17,500 geometries were created for training, development (hyperparameter optimization), and testing of the DL models. Additionally, mesh refinement was performed on 100 geometries by subdividing each tetrahedral element into eight smaller elements, resulting in meshes with 169,920 elements and 33,327 nodes. These refined meshes were used to assess the discretization invariance of our DL models.

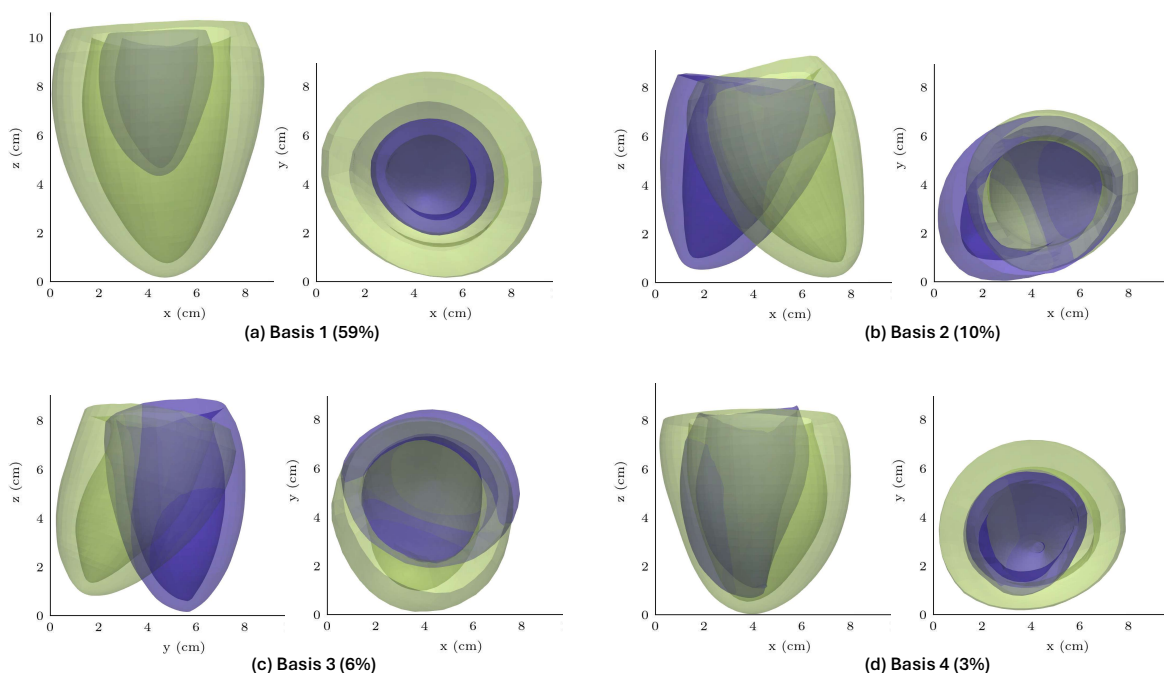


Figure 2: Illustration of the first four POD bases. Each panel illustrates the impact of adding the respective basis to the mean shape, using weights corresponding to the maximum (green) and minimum (blue) amplitudes identified by the POD analysis. Percentages in brackets indicate the variance represented by each base.

2.2 Governing equations of cardiac electrophysiology

Cardiac electrical activity and its propagation in the LV was described using the Aliev-Panfilov model [62]. This model employs two dimensionless state variables: the cardiac action potential ϕ and a recovery variable η , governed by

$$\frac{\partial \phi}{\partial t} = \nabla \cdot (\mathbf{D} \nabla \phi) + f_{\phi}(\phi, \eta) + I_s, \quad (1a)$$

$$\frac{\partial \eta}{\partial t} = f_{\eta}(\phi, \eta), \quad (1b)$$

where t represents the time elapsed since the beginning of systole. The anisotropic electrical conductivity tensor is defined as

$$\mathbf{D} = d_{\text{iso}}\mathbf{I} + d_{\text{ani}}\mathbf{f}_0 \otimes \mathbf{f}_0, \quad (2)$$

with d_{iso} and d_{ani} denoting the isotropic and anisotropic conductivities, respectively, and \mathbf{f}_0 denoting the myofiber direction vector. To reflect faster conduction along fibers, we set $d_{\text{ani}} = 4d_{\text{iso}}$, in line with literature values [63, 64]. In our simulations, d_{iso} was treated as a subject-specific parameter, and its value was randomly selected from the interval $[0.1, 2]$ to capture a wide range of outputs. The myofiber direction \mathbf{f}_0 , was prescribed to vary linearly across the myocardial wall, from 60° at the endocardium to -60° at the epicardium, using a Laplace-Dirichlet rule-based algorithm [61].

Local excitation was initiated by randomly selecting one or two pacing sites (radius up to 5 mm). A constant electrical stimulus I_s with a magnitude of 100 was applied at these locations between $t = 4$ ms and $t = 20$ ms. Single pacing-site simulations represented intrinsic activation associated with left branch bundle block (LBBB) [65], whereas dual pacing-site simulations modeled post-CRT scenarios, where the second pacing site represents the placed lead. The excitation properties of cardiac tissue are defined by

$$f_\phi(\phi, \eta) = -c\phi(\phi - \alpha)(\phi - 1) - \eta\phi, \quad (3a)$$

$$f_\eta(\phi, \eta) = \left(\gamma + \frac{\mu_1\eta}{\mu_2 + \phi} \right) (-\eta - c\phi(\phi - b - 1)), \quad (3b)$$

with the parameters associated with cellular-level dynamics set to $c = 8$, $\alpha = 0.01$, $\gamma = 0.002$, $\mu_1 = 0.2$, $\mu_2 = 0.3$, and $b = 0.15$, following [62]. Patient variability of these values was neglected. The activation time t_{act} at each spatial location $\mathbf{x} = (x, y, z)$ is computed as

$$t_{\text{act}}(\mathbf{x}) = \inf \{t(\mathbf{x}) | \phi(\mathbf{x}, t) \geq 0.9\}. \quad (4)$$

Prior to solving Eq. 1 for a generated geometry, the mesh quality was evaluated using the scaled Jacobian metric to identify and exclude unrealistic geometries. Specifically, geometries with more than 20% of elements exhibiting scaled Jacobian values below 0.1 were discarded. This conservative criterion resulted in approximately 12.5% (2,500 out of 20,000) geometry exclusion.

The governing equations Eq. 1 were solved using the FE method [15, 66]. Introducing $\mathbf{q} = \nabla\phi$ and using an implicit backward Euler time discretization (timestep $k = 0.08$), we solved the weak formulation to obtain $\phi \in \mathbf{H}^0(\Omega)$, $\mathbf{q} \in \mathbf{H}^1(\Omega)$, and $\eta \in \mathbf{H}^0(\Omega)$ such that

$$F_1 = \int_{\Omega} \frac{\phi - \phi_n}{k} \phi_{\text{test}} d\Omega - \int_{\Omega} \nabla \cdot (\mathbf{D}\mathbf{q}) \phi_{\text{test}} d\Omega - \int_{\Omega} f_\phi(\phi, \eta) \phi_{\text{test}} d\Omega - \int_{\Gamma} I_s \phi_{\text{test}} dS, \quad (5a)$$

$$F_2 = \int_{\Omega} \mathbf{q} \cdot \mathbf{q}_{\text{test}} d\Omega + \int_{\Omega} \phi \nabla \cdot \mathbf{q}_{\text{test}} d\Omega, \quad (5b)$$

$$F_3 = \int_{\Omega} \frac{\eta - \eta_n}{k} \eta_{\text{test}} d\Omega - \int_{\Omega} f_\eta(\phi, \eta) \eta_{\text{test}} d\Omega, \quad (5c)$$

are satisfied for all test functions $\phi_{\text{test}} \in \mathbf{H}^0(\Omega)$, $\mathbf{q}_{\text{test}} \in \mathbf{H}^1(\Omega)$, and $\eta_{\text{test}} \in \mathbf{H}^0(\Omega)$. Here, the domain Ω represents the LV geometry, and Γ denotes its surface.

Discontinuous Galerkin elements were employed to approximate ϕ and η , whereas Brezzi-Douglas-Marini (BDM) [67] were used for \mathbf{q} . Simulations spanned 200 ms (one-quarter cardiac cycle during cardiac depolarization), which are sufficient to capture a wide range of activation patterns, and were implemented using *FEniCS legacy* [68–70].

2.3 Geometric DL surrogate modeling

2.3.1 Input and output definitions

The input features, denoted by \mathbf{a} , include spatial coordinates (x, y, z) of a point cloud in the LV wall, a Boolean variable p_{pacing} specifying whether a point lies within a pacing site, the isotropic tissue electrical conductivity d_{iso} , and the myofiber direction vector $\mathbf{f}_0 = (f_{0x}, f_{0y}, f_{0z})$. The output, denoted by \mathbf{f} , is the activation time t_{act} corresponding to the point clouds. Specifically, for each point, we have

$$\mathbf{a} = (x, y, z, p_{\text{pacing}}, d_{\text{iso}}, f_{0x}, f_{0y}, f_{0z}), \quad \text{and} \quad \mathbf{f} = t_{\text{act}}. \quad (6)$$

In this study, d_{iso} remains homogeneous within each subject. The spatial coordinates (x, y, z) , conductivity (d_{iso}), and activation times (t_{act}) are scaled to Gaussian distributions with zero mean and unit variance.

2.3.2 Model architectures: GNN and GINO

GNN architecture. The GNN architecture employed in this study is based on GraphUNet [58], an extension of the widely used UNet architecture that was originally proposed for image segmentation [71]. UNet effectively captures global context through downsampling while preserving local information through skip connections during upsampling. GraphUNet adapts this approach to graph-structured data, enabling efficient learning on non-Euclidean domains.

We adopted the GraphUNet implementation by Bonnet *et al.* [72], developed for solving steady-state incompressible Navier-Stokes equations (Fig. 3). Network hyperparameters were chosen similarly, with specific adjustments tailored to our cardiac activation prediction task. The inputs to our model are the features \mathbf{a} (Eq. 6), along with local connectivity information established by linking points whose Euclidean distance is less than $r = 2.5$ mm.

Initially, node features are mapped to an embedding dimension d_{emb} , through a four-layer multilayer perceptron (MLP) with 256 neurons per layer, where d_{emb} is determined through hyperparameter optimization. Subsequently, node embeddings are updated using SageConv (GraphSAGE) layers [73], which aggregate information from neighboring nodes as follows

$$\mathbf{z}_i^{(\ell)} = \mathbf{W}_1 \mathbf{z}_i^{(\ell-1)} + \mathbf{W}_2 \left(\frac{1}{|\mathcal{N}(i)|} \sum_{j \in \mathcal{N}(i)} \mathbf{z}_j^{(\ell-1)} \right), \quad (7)$$

where $\mathbf{z}_i^{(\ell-1)}$ and $\mathbf{z}_i^{(\ell)}$ are the input and output embeddings of node i at layer ℓ , respectively, $\mathcal{N}(i)$ denotes the set of neighboring nodes, and \mathbf{W}_1 and \mathbf{W}_2 are learnable weight matrices.

In the downsampling path, after each SageConv layer, a fraction of points is retained randomly (specifically, $\frac{3}{4}$, $\frac{3}{4}$, $\frac{2}{3}$, and $\frac{2}{3}$), and connectivity is recalculated with updated neighborhood radius r of 3.75, 7.5, 12.5, and 20 mm, respectively. During training, a maximum of 32 neighbors per node are considered to reduce computational cost, while during inference, this limit increases to 256 neighbors to capture richer local information and improve prediction accuracy.

Each SageConv layer in the downsampling path doubles the channel dimension (from d_{emb} up to $16d_{\text{emb}}$), which is subsequently halved in the upsampling path. Skip connections ensure detailed local information is preserved during the reconstruction phase. Each

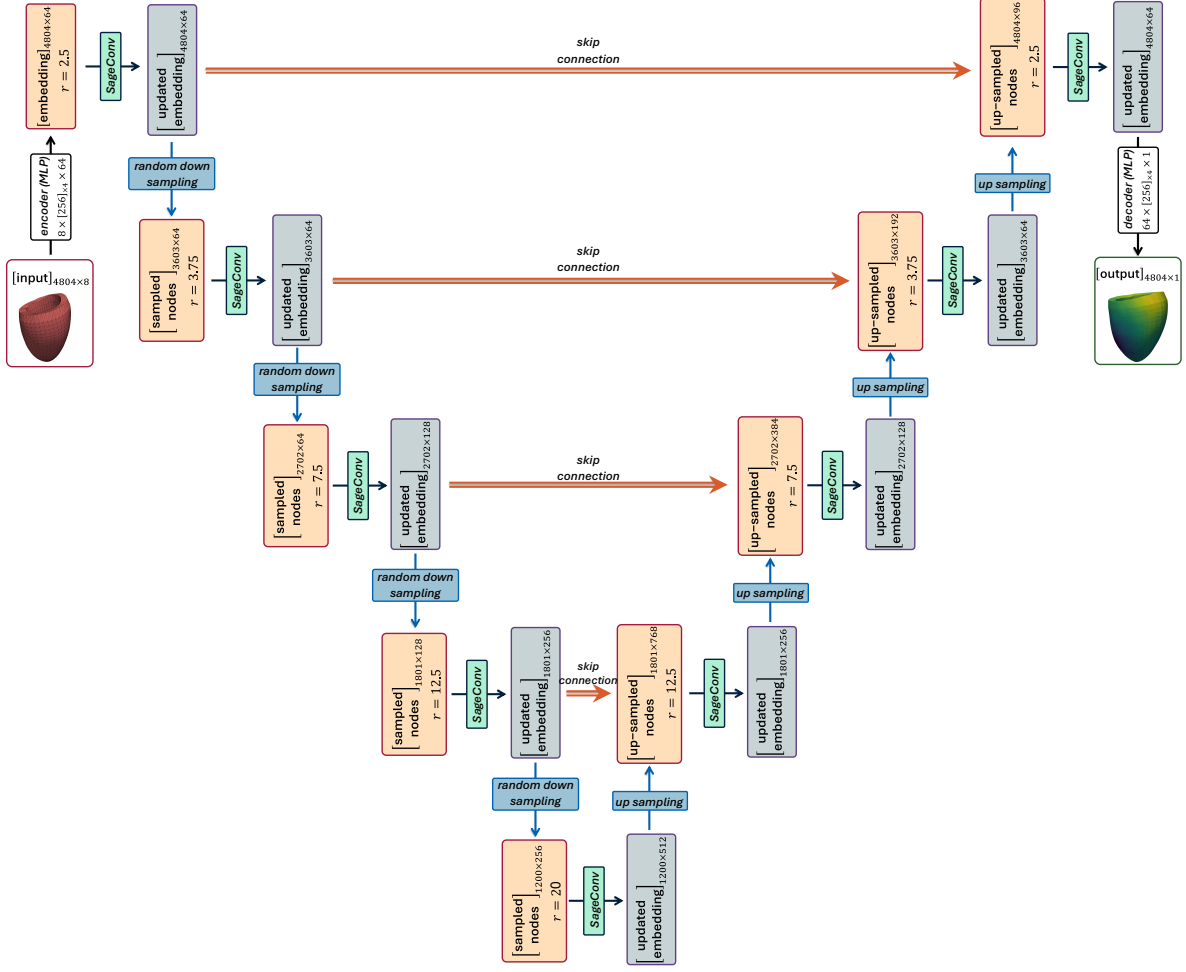


Figure 3: Graph-UNet architecture for $d_{emb} = 64$. The dimension of 4804 points per case assumes a batch size of 1 here for illustration purposes only, and does not represent a structural limitation of the network.

SageConv layer is followed by batch normalization and a ReLU activation function. A final decoder MLP maps the node embeddings back to the scalar activation times.

GINO architecture. The GINO architecture adopted in this study is based on the formulation by Li *et al.* [59] (Fig. 4). Neural operators generalize traditional feed-forward neural networks (FNNs), transitioning from mappings between finite-dimensional vectors to mappings between infinite-dimensional function spaces. Similar to FNNs, which consist of sequential linear transformations (e.g., matrix multiplications or convolutions) followed by pointwise nonlinear activations, neural operators incorporate sequences of linear operators combined with pointwise nonlinearities.

To formalize the neural operator, we consider an operator

$$\Psi : \mathcal{A} \rightarrow \mathcal{U}, \quad (8)$$

mapping between function spaces \mathcal{A} and \mathcal{U} . The neural operator Ψ_θ is constructed to estimate Ψ with $L + 2$ layers, expressed as

$$\Psi_\theta := \mathcal{G}_{L+1} \circ \mathcal{G}_L \circ \cdots \circ \mathcal{G}_1 \circ \mathcal{G}_0, \quad (9)$$

where \mathcal{G}_0 is the initial lifting operator mapping inputs to a higher-dimensional space, and \mathcal{G}_{L+1} is the projection operator mapping to the output space. Both operators act pointwise and are typically parameterized by MLPs.

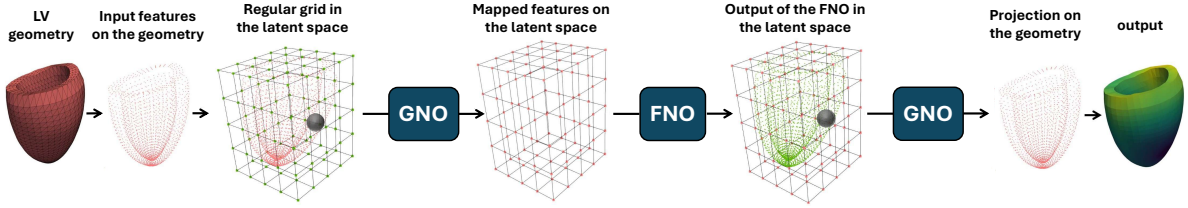


Figure 4: Schematic of the GINO architecture. The input LV geometry, discretized into a point cloud, is mapped onto a regular latent grid using the GNO encoder. For each node in the latent grid, a ball with radius r aggregates features from points of the original geometry falling within this radius. This latent representation is subsequently processed by an FNO model. Finally, the resulting latent features are interpolated back onto the original geometry via the GNO decoder, where, for each original geometry point, features are gathered from adjacent nodes within a radius r in the latent space.

Each intermediate layer $\mathcal{G}_\ell : v_{\ell-1}(x) \rightarrow v_\ell(x)$ (for $\ell = 1, 2, \dots, L$) is described by

$$v_\ell(x) = \sigma\left(W_\ell v_{\ell-1}(x) + \mathcal{K}_\ell(v_{\ell-1})(x) + b_\ell\right), \quad (10)$$

where σ denotes a pointwise nonlinear activation, W_ℓ and b_ℓ are the weight and the bias parameters, which are set to be constant functions here as in standard neural networks. We note W_ℓ and b_ℓ can also be arbitrary functions (e.g. MLPs). \mathcal{K}_ℓ is a linear operator differentiating neural operators from FNNs, enabling mappings between function spaces and is represented in integral form

$$\mathcal{K}_\ell(v_{\ell-1})(x) = \int_D \kappa_\ell(x, y) v_{\ell-1}(y) dy, \quad (11)$$

where D is the domain of $v_{\ell-1}$, and κ_ℓ is a kernel function. To better capture nonlinear interactions, the kernel function κ_ℓ in Eq. 11 can be extended to depend on the input function $v_{\ell-1}$ as follows

$$\mathcal{K}_\ell(v_{\ell-1})(x) = \int_D \kappa_\ell(x, y, v_{\ell-1}(x), v_{\ell-1}(y)) v_{\ell-1}(y) dy. \quad (12)$$

The kernel function κ_ℓ is parameterized and learned during training along with the weights (W_ℓ) and biases (b_ℓ). Two prominent approaches are:

- **Graph neural operator (GNO):** GNO [74], localizes Eq. 12 by truncating the domain to a ball of radius r around each point x

$$\mathcal{K}_\ell(v_{\ell-1})(x) = \int_{B_r(x)} \kappa_\ell(x, y, v_{\ell-1}(x), v_{\ell-1}(y)) v_{\ell-1}(y) dy. \quad (13)$$

Discretizing this integral via a Nyström approximation yields

$$\mathcal{K}_\ell(v_{\ell-1})(x) \approx \sum_{i=1}^M \kappa_\ell(x, y_i, v_{\ell-1}(x), v_{\ell-1}(y_i)) v_{\ell-1}(y_i) \mu(y_i), \quad (14)$$

where $\{y_1, y_2, \dots, y_M\} \subset B_r(x)$ and $\mu(y_i)$ are Riemannian sum weights. This formulation corresponds to a message-passing framework on graphs [75].

- **Fourier neural operator (FNO):** FNO simplifies $\kappa_\ell(x, y, v_{\ell-1}(x), v_{\ell-1}(y)) := \kappa_\ell(x - y)$, and by applying the convolution theorem, the integral operator in Eq. 12 can be computed efficiently in the Fourier domain as [76]

$$\mathcal{K}_\ell(v_{\ell-1})(x) = \mathcal{F}^{-1}\left(R_\ell \cdot \mathcal{F}(v_{\ell-1})\right)(x), \quad (15)$$

where \mathcal{F} and \mathcal{F}^{-1} denote the Fourier and inverse Fourier transforms, respectively, and R_ℓ is the Fourier representation of the kernel κ_ℓ . κ_ℓ is assumed to be periodic (by padding the input with zeros) to enable working with the discrete Fourier modes. In practice, when the input grid is uniform, the discrete Fourier transform (computed via fast Fourier transform [77]) is employed.

GNO handles arbitrary geometries but may struggle with problems that involve long-range dependencies [78], whereas FNO captures global interactions but is computationally efficient only on regular grids [76]. GINO captures the advantages of both through the integration of three main components:

- **GNO encoder:** The GNO encoder maps input LV point cloud features onto a latent regular grid via local integrals discretized as

$$\mathbf{a}(x^{\text{grid}}) \approx \sum_{i=1}^M \kappa(x^{\text{grid}}, y_i^{\text{in}}) \mathbf{a}(y_i^{\text{in}}) \mu(y_i^{\text{in}}), \quad (16)$$

where the integration is performed over the ball $B_{r_{\text{in}}}(x^{\text{grid}})$. The Riemannian weights $\mu(y_i^{\text{in}})$ are computed to account for the local density of points.

- **FNO core:** The FNO model processes latent representations on the regular grid $\mathbf{a}(x^{\text{grid}})$ efficiently capturing global interactions by operating in Fourier space.
- **GNO decoder:** The GNO decoder interpolates the latent grid back to the original LV geometry via local integrals discretized as

$$u(x^{\text{out}}) \approx \sum_{i=1}^S \kappa(x^{\text{out}}, y_i^{\text{grid}}) u(y_i^{\text{grid}}) \mu(y_i^{\text{grid}}), \quad (17)$$

where $\{y_1^{\text{grid}}, y_2^{\text{grid}}, \dots, y_S^{\text{grid}}\} \subset B_{r_{\text{out}}}(x^{\text{out}})$. In this step, since the latent grid is regular, the Riemannian weights are set uniformly.

Hyperparameters in the GINO model are prescribed following [59], except the number of Fourier modes (m) was optimized via hyperparameter tuning. The latent resolution was 32^3 , and the local integration radius was set to $r = 2.5$ mm.

2.3.3 Training and metrics

The 17,500 simulation cases were split into three sets: one with 8,700 cases for training and two with 4,400 cases each for development (hyperparameter optimization, abbreviated as “dev”) and testing. Additionally, 100 cases with a refined discretization were used to assess the discretization invariance of the trained models.

To quantify model performance at both regional (pointwise) and aggregate (subject-level) scales, two metrics were employed. The local absolute error at point i is defined as

$$e_i = |\hat{t}_{\text{act}} - t_{\text{act}}|_i, \quad (18)$$

where \hat{t}_{act} is the model prediction, and t_{act} is the ground truth from FE simulation. For each case k , the global relative error is calculated as

$$E_k = \left(\frac{\frac{1}{n} \sum_{i=1}^n |\hat{t}_{\text{act}} - t_{\text{act}}|_i}{\frac{1}{n} \sum_{i=1}^n (t_{\text{act}})_i} \right)_k, \quad (19)$$

where n denotes the total number of sampled points in case k . The loss for a batch B is defined by the mean global error

$$\mathcal{L}_B = \frac{1}{|B|} \sum_{k=1}^{|B|} E_k. \quad (20)$$

We added mini-batch support to the reference implementations of both models and for each model, chose the largest batch size $|B|$ that fits the GPU memory. To evaluate model robustness against input noise, Gaussian perturbations at levels of 1%, 5%, 10%, 15%, and 20% of the channel-wise standard deviation were added to the coordinates (x, y, z) and fiber directions $(f_{0_x}, f_{0_y}, f_{0_z})$ in the test dataset.

The models were developed using *PyTorch* [79], *Torch Geometric* [80], and *Neural Operator* [55, 81]. Both GNN and GINO models were trained using the AdamW optimizer [82] with an initial learning rate of 10^{-3} , and a `ReduceLROnPlateau` learning rate scheduler that halves the learning rate after 50 stagnant epochs, down to a minimum of 10^{-6} .

2.4 Clinical application in CRT planning

We illustrated post-training application of this study in CRT planning with a baseline case that had one intrinsic pacing site and a prolonged maximum activation time (pathologic scenario associated with LBBB). Given the LV geometry and a measured activation map (simulated here but clinically measurable), we first estimated the isotropic conductivity d_{iso}^* , and the intrinsic pacing site $p_{\text{pacing}_1}^*$ by solving

$$\left(d_{\text{iso}}^*, p_{\text{pacing}_1}^* \right) = \arg \min_{(d_{\text{iso}}, p_{\text{pacing}_1})} (E_k). \quad (21)$$

With these personalized parameters fixed, we then searched for the optimal CRT lead position $p_{\text{pacing}_2}^*$ to minimize the maximum activation time,

$$p_{\text{pacing}_2}^* = \arg \min_{p_{\text{pacing}_2}} \left(\max (t_{\text{act}}(\mathbf{x})) \right). \quad (22)$$

Reduction in maximum activation time has been shown in prior studies to correlate with improved CRT response [83–85]. Both optimization problems (Eqs. 21-22) were

solved using the differential evolution method [86, 87] as implemented in *SciPy* [88]. This evolutionary approach was selected over the gradient-based methods, which are prone to converging to local optima.

For consistent and interpretable reporting, pacing sites were described using reduced prolate-spheroidal coordinates (x_t, x_c, x_l) [89], with $x_t \in [0, 1]$ denoting transmural position (0 = epicardium, 1 = endocardium), $x_c \in [-\pi, \pi]$ denoting circumferential position (0 at the inferior valve-ring intersection, increasing counter-clockwise when viewed from the apex), and $x_l \in [0, 1]$ representing longitudinal position (apex \rightarrow base). Detailed implementation can be found in [32].

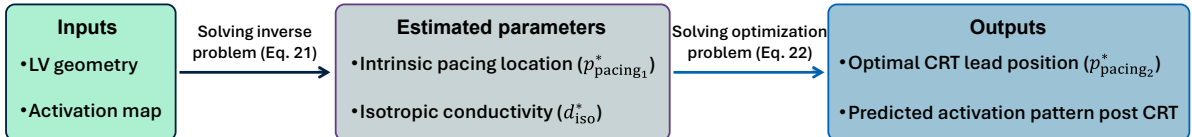
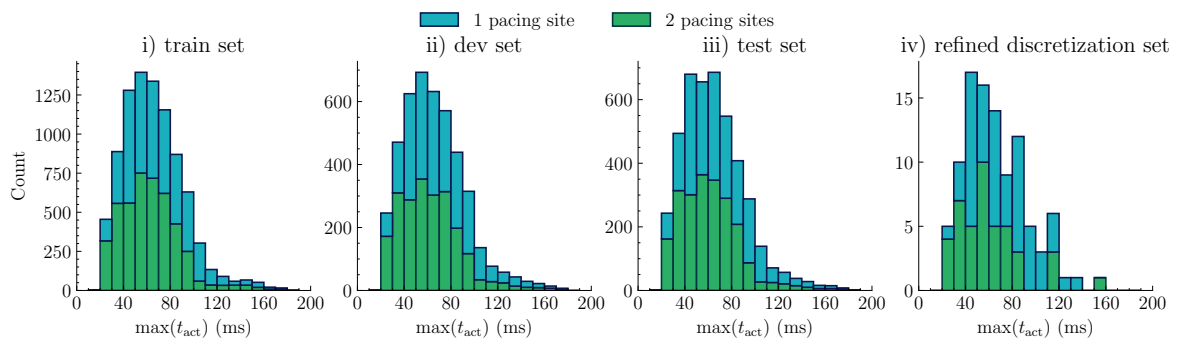


Figure 5: CRT optimization workflow

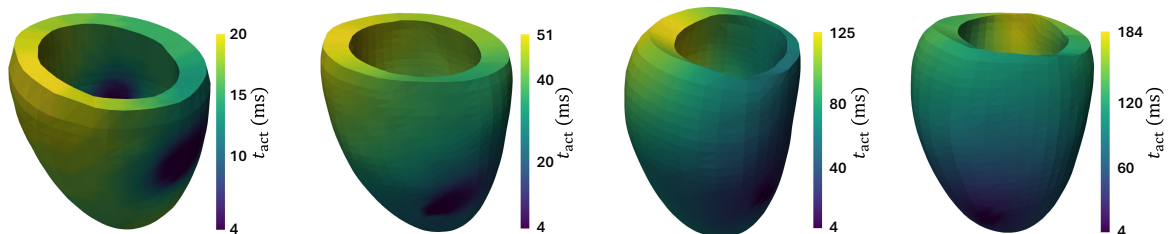
3 Results

3.1 Characteristics of the generated dataset

Each FE simulation required approximately 12 minutes of computational time on a single CPU core. By running 17,500 simulations concurrently across 1,000 cores on the Michigan State University High-Performance Computing Cluster (HPCC), all simulations were completed in 8 hours.



(a) Histogram of maximum activation times across the dataset. Panels i) – iii) represent training, dev, and test splits, respectively. Panel iv) illustrates the refined discretization set.



(b) Examples of activation patterns

Figure 6: FE simulation results

Fig. 6 shows the histograms of maximum activation times observed in the dataset and examples of the resulting activation patterns from FE simulations. Activation times range

from 19 ms to 184 ms, with 95% of cases falling between 30 ms and 120 ms. Half of the simulations are associated with one pacing site, whereas the remaining half is associated with two pacing sites that correspond to post-CRT scenarios.

3.2 Performance analysis of GNN and GINO models

Both DL models were trained on four Nvidia H200 Tensor Core GPUs at the Michigan State University HPCC. To determine the optimal architecture for each model, the embedding dimension d_{emb} of the GNN model was varied from 16 to 128, whereas the number of Fourier modes m per spatial direction in the GINO model was varied from 4 to 32. Each candidate model was trained for approximately 2,000 epochs, retaining the checkpoint with the lowest dev loss.

Table 1 shows the performance of the GNN model with d_{emb} . The GNN model is optimal with $d_{emb} = 64$, where the dev loss is at the minimum. Similarly, Table 2 shows the performance of the GINO model with m . For GINO, increasing Fourier modes beyond $m = 8$ yielded minimal improvements in dev loss but significantly increased the number of parameters. Since dev losses were similar for models with 8 or more Fourier modes, we examined the performance on the refined discretization set, finding a noticeable improvement moving from 8 to 16 modes but only marginal gains beyond 16 modes. Consequently, we selected $m = 16$ as the optimal GINO configuration. Table 3 summarizes the performance of the optimized GNN and GINO models, showing consistently lower errors from the GINO model across all datasets. Notably, even the smallest GINO model ($m = 4$) outperformed the optimal GNN model.

Table 1: GNN hyperparameter optimization. Models with different embedding widths d_{emb} , trainable parameter counts, and batch sizes. \mathcal{L} is the mean relative error (Eq. 20) over each set. Boldface marks the lowest dev loss.

d_{emb}	# params (million)	batch size	\mathcal{L}	
			train	dev
16	0.63	254	0.0414	0.0431
32	1.29	169	0.0296	0.0334
64	3.93	84	0.0265	0.0317
128	14.4	33	0.0267	0.0326

Table 2: GINO hyperparameter optimization. Models with different number of Fourier modes m per spatial direction, trainable parameter counts, and batch sizes. The “refined” column reports error on refined discretization set. The configuration in boldface was selected, balancing dev loss, refined loss, and parameter count.

m	# params (million)	batch size	\mathcal{L}		
			train	dev	refined
4	0.97	148	0.0130	0.0142	0.0259
8	8.64	127	0.0098	0.0117	0.0306
16	66.7	97	0.0081	0.0116	0.0270
32	476.7	76	0.0080	0.0114	0.0268

Table 3: Comparison of the optimal GNN and GINO models. Columns list number of trainable parameters, wall-clock training time on four GPUs, and errors \mathcal{L} on each dataset (train, dev, test, refined).

model	# params (million)	training time (hour)	\mathcal{L}			
			train	dev	test	refined
GNN	3.93	12	0.0265	0.0317	0.0314	0.1068
GINO	66.7	20	0.0081	0.0116	0.0114	0.0270

Fig. 7 assesses the robustness of both models to input noise on the test set and their performance on the refined discretization set. Without added noise, the GINO model produced errors below 2% for 75% of the predictions, with maximum errors below 15%. The GNN showed errors below 4% for 75% of cases, with exhibited maximum errors approaching 20%. Both models were stable under noise conditions, with errors lower than or comparable to the introduced noise level. On the refined discretization set, the GINO model maintained its performance, with errors rarely exceeding 4% in 75 out of 100 cases. Conversely, the GNN model produced an average error exceeding 10%.

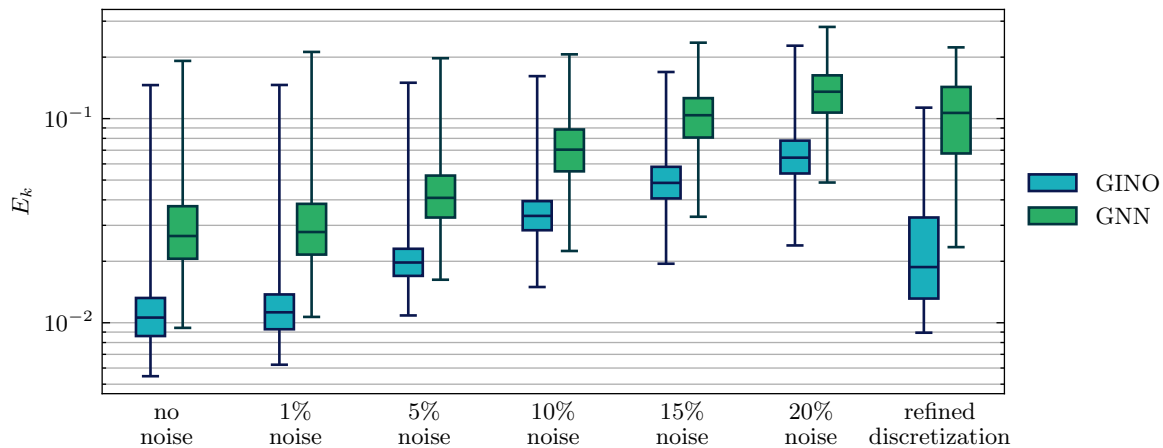


Figure 7: Test set errors for the GNN and GINO models, with no noise and with Gaussian perturbations of 1% – 20%. The rightmost boxes show performance on the refined discretization set. Whiskers were extended to the minimum and maximum observed errors.

Fig. 8 shows the variation of prediction errors across subjects with different maximum activation times and between cases with one or two pacing sites. The GINO model generally performed better in single-pacing-site scenarios, with larger errors corresponding to the activation times where fewer training samples were available (see Fig. 6a). The GNN model has a larger prediction error than the GINO model. There is no clear trend in the prediction error, however, with respect to the pacing configuration or activation time.

Figs. 9 and Fig. 10 compare predictions from the GNN and GINO models with the FE simulation ground truths, respectively. For each model, two typical examples (one and two pacing sites) are shown alongside the two cases with the highest global errors. The GINO model consistently captured the overall activation patterns accurately, with the largest error primarily localized near the pacing sites, even in cases with high global error. The GNN showed comparable performance for typical cases but exhibited substantial discrepancies in some cases, with large errors extending well beyond the vicinity of the pacing sites.

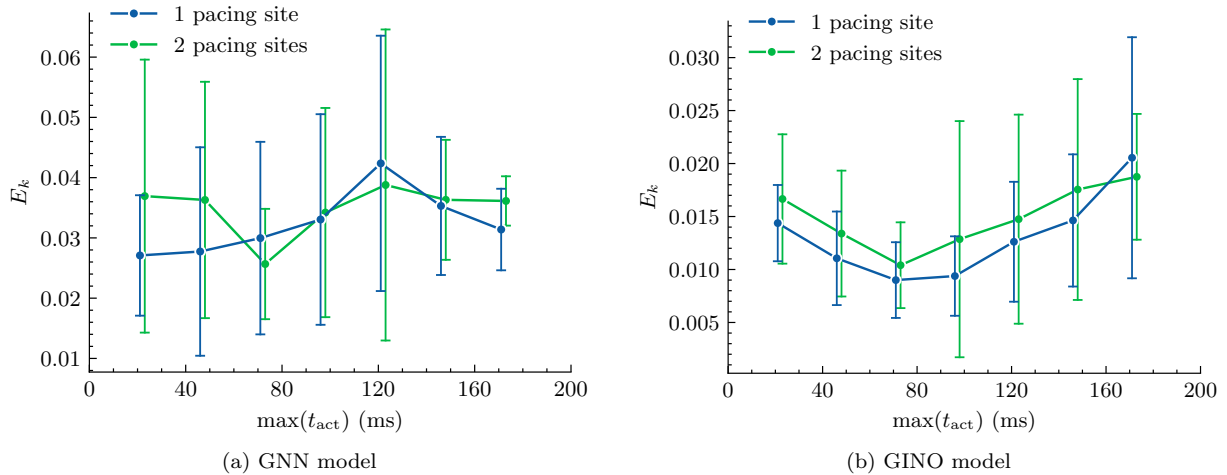


Figure 8: Variation in error as a function of maximum activation time and number of pacing sites.

3.3 Application case: CRT patient simulation

Given the superior performance of the trained GINO model as a surrogate for the FE solution, compared to the GNN model, it was used in the CRT optimization workflow described in Fig. 5. The results of the workflow are illustrated in Fig. 11 and summarized numerically in Tables 4 and 5. The test case chosen to illustrate the workflow had a single intrinsic pacing site and a prolonged maximum activation time of 147 ms, reflecting pathological conditions associated with LBBB. Clinically, a measured activation map from the patient would be used instead of the simulated one presented here.

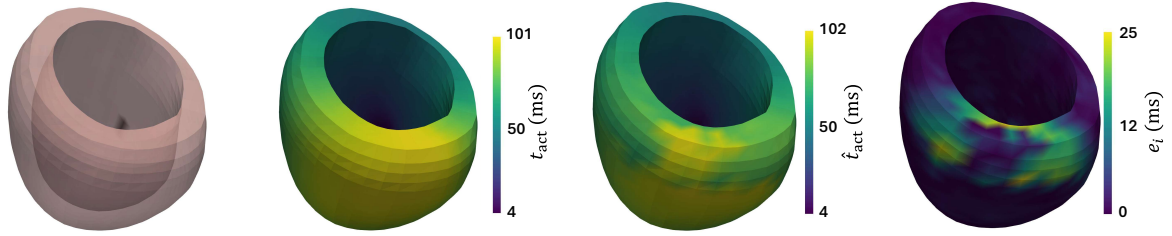
The estimated values for the tissue conductivity d_{iso} and intrinsic pacing site p_{pacing_1} differed from the ground truth by 4.3% and 1.8%, respectively. With these personalized parameters fixed, solving Eq. 22 showed that pacing at the optimized site reduced the maximum activation time by 20% (from 147 ms to 118 ms). In contrast, pacing at a randomly chosen site resulted in only an 8% reduction (to 135 ms). The optimization workflow was completed within 2 minutes.

Table 4: Results of the inverse problem. Estimated vs. true values for the first pacing site coordinates (x_l, x_c) and isotropic conductivity d_{iso} .

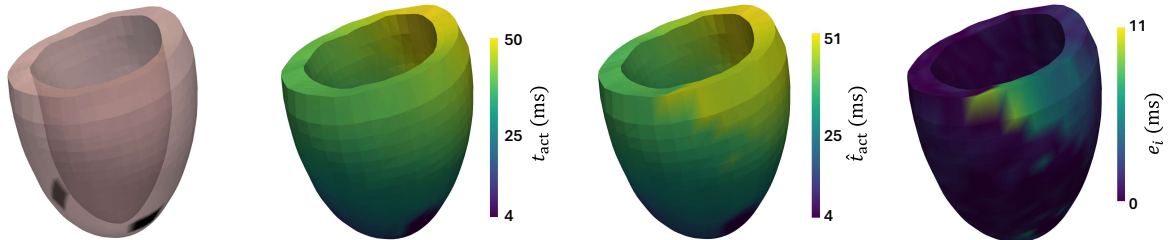
	x_l	x_c	d_{iso}
Ground truth	0.3248	-2.8533	0.1269
Estimated	0.3236	-2.9022	0.1324
Error (%)	0.4%	1.7%	4.3%

Table 5: CRT pacing-site optimization results. Comparison of maximum activation times achieved by random vs. optimized second pacing site placement.

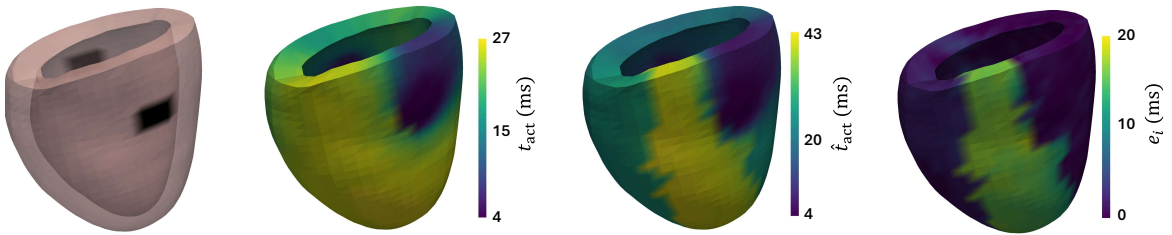
	x_l	x_c	$\max(t_{\text{act}})$ (ms)
Baseline (single site)	–	–	147
Random second site	0.5431	0.6678	135
Model-optimized second site	0.4328	1.3708	118



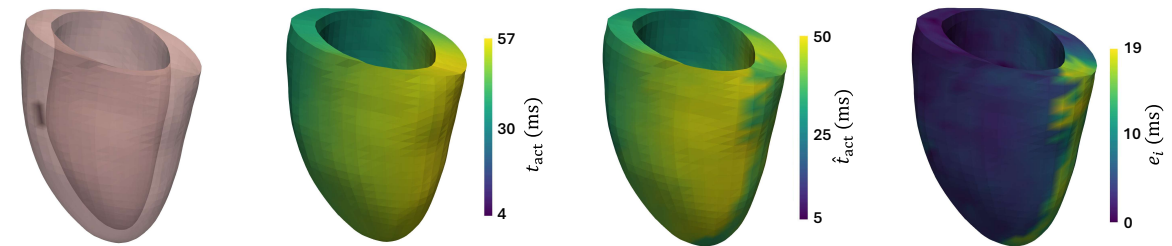
(a) A sample case with one pacing site. The global error (E_k) for this case is 0.0287.



(b) A sample case with two pacing sites. The global error (E_k) for this case is 0.0291.

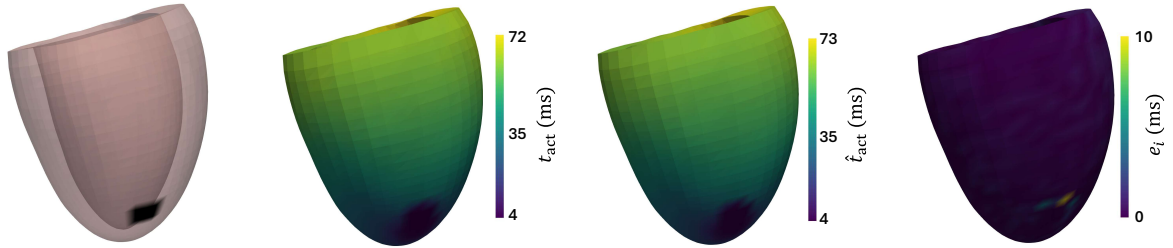


(c) The case with the largest global error ($E_k = 0.2027$) in the test set.

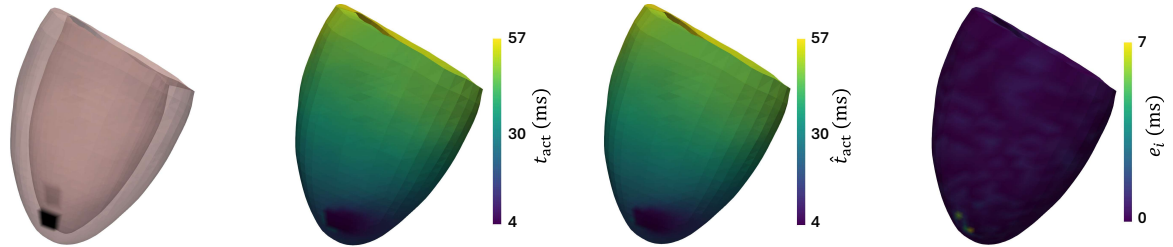


(d) The case with the second largest global error ($E_k = 0.1815$) in the test set.

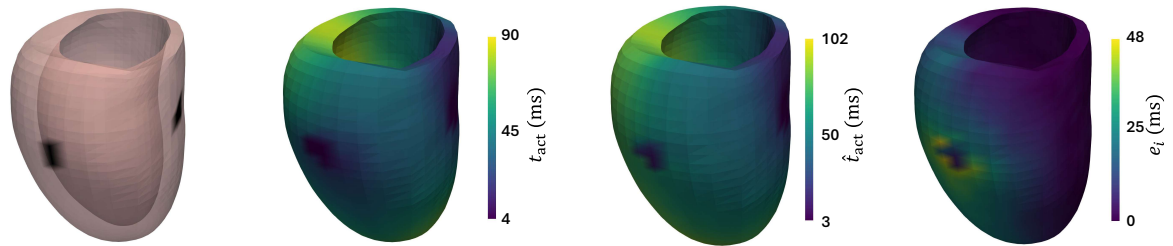
Figure 9: Sample results illustrating the GNN model predictions and errors. From left to right, the panels show: the pacing site(s), the activation pattern from the FE simulation (t_{act}), the activation pattern from the GNN model prediction (\hat{t}_{act}), and the local error (e_i).



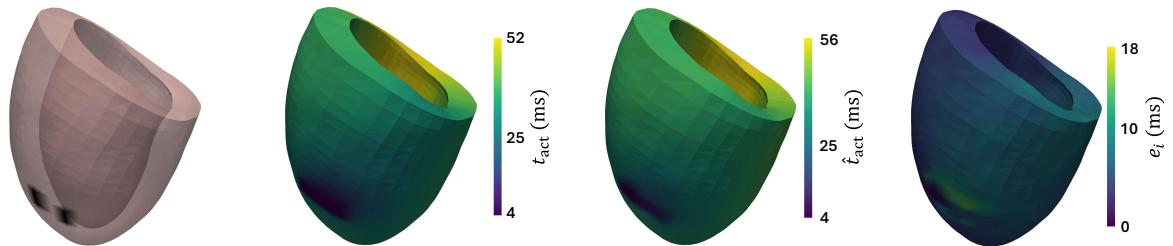
(a) A sample case with one pacing site. The global error (E_k) for this case is 0.0079.



(b) A sample case with two pacing sites. The global error (E_k) for this case is 0.0108.



(c) The case with the largest global error ($E_k = 0.1459$) in the test set.



(d) The case with the second largest global error ($E_k = 0.1194$) in the test set.

Figure 10: Sample results for the GINO. Refer to Fig. 9 for organization.

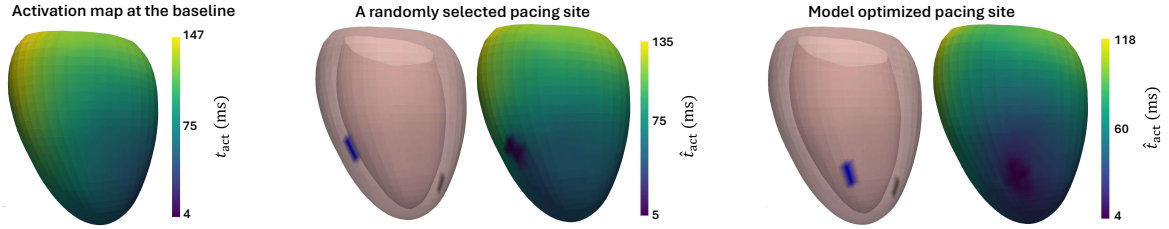


Figure 11: Example CRT optimization using the GINO model. Left panel: Baseline activation map from the FE simulation (clinically, this map could be measured). Center panel: Activation map for a randomly selected pacing site. Right panel: Activation map for the model-optimized pacing site. The intrinsic pacing site is marked in black, whereas candidate second pacing sites are indicated in blue.

4 Discussion

The key finding here is that GINO model is superior to GNN in terms of accuracy and robustness to noise and variation in discretization. Using the GINO model, we developed a workflow to demonstrate its applicability for subject-specific CRT optimization, which can potentially reduce the rate of CRT non-responders.

4.1 Comparative advantages of GINO over GNN

The GINO model consistently outperforms the Graph-UNet GNN model across all evaluation metrics (Fig. 7 and Table 3). It is widely acknowledged that training GNN models is complex, with optimal architectures varying significantly based on the application [90–92]. Common challenges associated with GNN models include over-smoothing, wherein repeated neighborhood aggregation diminishes the distinctiveness of node embeddings [93, 94]. Likewise, over-squashing, where messages from distant nodes become overly compressed, in turn limits the capture of long-range dependencies [95]. Despite Graph-UNet attempts to mitigate these issues through skip connections and downsampling, the trained GNN model frequently shows significant deviations from the FE ground truths (Fig. 9). In contrast, the GINO model is inherently less susceptible to issues associated with the GNN model, yielding significantly lower overall prediction errors (1.14% vs 3.14%). While the GINO model occasionally exhibits large local errors near the pacing sites, it can still predict the overall activation patterns even in cases with the largest errors (Fig. 10). These results underscore the benefits of the operator-based DL approach for cardiac activation prediction.

Between pacing configurations, the GINO model performs better in scenarios with a single pacing site compared to those with two pacing sites (Fig. 8). Random selection occasionally placed the two pacing sites close to each other, making the resulting activation pattern from the FE simulation more challenging to learn than in most other cases. Despite the higher error in this configuration, the model is still able to capture the overall activation pattern, with larger errors appearing only near the pacing sites (Fig. 10d). We note that this configuration is unlikely to occur in CRT planning, as pacing is typically performed away from the earliest activated region (corresponding to a pacing site here). Nevertheless, such configurations were retained to ensure unbiased representation within the dataset. In comparison, the GNN’s higher baseline errors obscure any clear distinctions between single- and dual-site scenarios.

4.2 Comparison with prior physics-based DL models on arbitrary geometries

The error levels achieved by our DL models fall within the range reported in previous studies. The original GINO study [59], a recent transformer-based approach [96], and the GNN-based DrivAerNet [97], all reported mean test errors between 2% and 10% for Navier-Stokes flow simulations around vehicle bodies.

Compared to the neural operator framework proposed by Yin *et al.* [57], which was trained on data from FE simulations of a monodomain reaction-diffusion model to predict activation patterns in the LV and reported a prediction error of 0.04, both the GNN and GINO models presented here achieve lower errors of 0.0314 and 0.0114, respectively. Although their model is considerably more efficient to train (completed in approximately 12 minutes on a single GPU using 2 GB of memory, compared to 20 hours for our GINO model on four NVIDIA H200 GPUs with 140 GB each), inference in both models runs in real time with negligible latency. In addition, the DL models presented here operate directly on point cloud representations of LV geometries, whereas Yin *et al.*'s framework relies on principal component analysis (PCA) for geometry encoding, a dimensionality reduction technique that may struggle to capture local geometric features.

4.3 Clinical implications for CRT planning

The computational efficiency of the trained GINO model, which predicts activation maps in just a few milliseconds (cf. to ~ 12 mins in FE simulations), makes it feasible to be used for solving optimization problems, where numerous pacing sites are evaluated to identify the optimal lead position. To demonstrate this utility, we developed a workflow that identifies the optimal lead position with the LV geometry and corresponding activation time map as inputs (Fig. 5). We note that the LV geometry can be reconstructed from 3D echocardiography and the activation time map can be measured from electroanatomical mapping in clinical practice. Optimization of the CRT pacing site is completed within 2 minutes, despite solving two optimization problems (Eqs. 21-22) using an evolutionary algorithm with thousands of evaluations. The optimal pacing site yielded a 20% reduction in maximum activation time (147 ms \rightarrow 118 ms), whereas a randomly chosen site achieved only an 8% reduction. To increase the accessibility of GINO model, we also developed a web-based interactive GUI (<https://dcsim.egr.msu.edu/>) allowing users to upload patient-specific LV geometries, evaluate pacing scenarios interactively in real time, and visualize predicted activation maps. This demonstrates the model's potential as a practical clinical decision-support tool. This developed workflow sets the foundation for in-silico optimization of CRT, and continuous updates to this GUI will be provided as newer, more expressive backend DL models are developed.

4.4 Limitations and future work

We note a few limitations in this study, which point to areas for future improvement. **First**, the LV geometries used to train the DL models were synthesized using the POD model described by Buoso *et al.* [32]. While the POD model was based on 75 LV geometries derived from healthy individuals and patients with cardiovascular diseases, it may not capture the full spectrum found in patients with LBBB and other heart diseases. Therefore, the model's performance on geometries derived from other sources, such as patient-specific clinical data, needs further validation. **Second**, the DL models focus

only on cardiac electrophysiology and do not consider mechanical deformation, which is also an important aspect to consider when optimizing CRT. Future DL models will consider cardiac electromechanics by either training them using generated simulation dataset derived from fully coupled electromechanical LV models or using physics-informed training methods that could substantially reduce the required volume of pre-computed data [98]. Incorporating differential-equation constraints into the loss function of neural operators such as GINO, however, remains technically challenging [99, 100]. **Third**, we assumed that the activation time map associated with LBBB can be reproduced from a single pacing site along with the tissue conductivity. This may not be the case especially when there are multiple confounding factors such as ischemia that can affect tissue conductivity locally. The DL models can be refined further by considering more pacing locations and local variation in the tissue conductivity.

5 Summary and conclusions

In summary, we compared two physics-based DL models, namely Graph-UNet based GNN and GINO, and showed that the latter model is superior in terms of its accuracy and robustness to predict activation patterns across diverse LV geometries and pacing configurations. We further demonstrated the practical clinical utility of GINO model for in-silico optimization of the pacing site in CRT planning and its accessibility through an interactive web-based GUI that enables users to visualize and evaluate different pacing scenarios in real-time. This study sets the foundation for our future work to improve its generalizability to clinical patient-specific geometries and the consideration of cardiac electromechanics in our models.

Acknowledgement

This work was supported by NIH R01HL166508, R43HL174177 and NSF 2406029.

Code and data availability

The code and the data are available at <https://github.com/ehsanng/DeepCardioSim>.

Declaration of competing interest

The authors declare that they have no known competing financial interests or personal relationships that could have appeared to influence the work reported in this paper.

References

- [1] M. Glikson, J. C. Nielsen, M. B. Kronborg, Y. Michowitz, A. Auricchio, I. M. Barbash, J. A. Barrabés, G. Boriani, F. Braunschweig, M. Brignole, H. Burri, A. J. S. Coats, J.-C. Deharo, V. Delgado, G.-P. Diller, *et al.*, “Corrigendum to: 2021 ESC guidelines on cardiac pacing and cardiac resynchronization therapy: Developed by the task force on

- cardiac pacing and cardiac resynchronization therapy of the European Society of Cardiology (ESC): With the special contribution of the European Heart Rhythm Association (EHRA),” *EP Europace*, vol. 24, no. 4, pp. 699–699, Mar. 2022 (cit. on p. 2).
- [2] N. D. Almeida, E. Suarathana, N. Dendukuri, and J. M. Brophy, “Cardiac resynchronization therapy in heart failure: Do evidence-based guidelines follow the evidence?” *Circulation: Cardiovascular Quality and Outcomes*, vol. 10, no. 12, e003554, 2017 (cit. on p. 2).
- [3] F. A. McAlister, J. Ezekowitz, N. Hooton, B. Vandermeer, C. Spooner, D. M. Dryden, R. L. Page, M. A. Hlatky, and B. H. Rowe, “Cardiac resynchronization therapy for patients with left ventricular systolic dysfunction a systematic review,” *JAMA*, vol. 297, no. 22, pp. 2502–2514, Jun. 2007 (cit. on p. 2).
- [4] W. T. Abraham, W. G. Fisher, A. L. Smith, D. B. Delurgio, A. R. Leon, E. Loh, D. Z. Kocovic, M. Packer, A. L. Clavell, D. L. Hayes, M. Ellestad, R. J. Trupp, J. Underwood, F. Pickering, C. Truex, *et al.*, “Cardiac resynchronization in chronic heart failure,” *New England Journal of Medicine*, vol. 346, no. 24, pp. 1845–1853, 2002 (cit. on p. 2).
- [5] C. Ypenburg, R. J. van Bommel, C. J. W. Borleffs, G. B. Bleeker, E. Boersma, M. J. Schalij, and J. J. Bax, “Long-term prognosis after cardiac resynchronization therapy is related to the extent of left ventricular reverse remodeling at midterm follow-up,” *Journal of the American College of Cardiology*, vol. 53, no. 6, pp. 483–490, 2009 (cit. on p. 2).
- [6] N. Wijesuriya, M. K. Elliott, V. Mehta, F. De Vere, M. Strocchi, J. M. Behar, S. A. Niederer, and C. A. Rinaldi, “Pacing interventions in non-responders to cardiac resynchronization therapy,” *Frontiers in Physiology*, vol. 14, 2023 (cit. on p. 2).
- [7] P. C. Wouters, K. Vernooij, M. J. Cramer, F. W. Prinzen, and M. Meine, “Optimizing lead placement for pacing in dyssynchronous heart failure: The patient in the lead,” *Heart Rhythm*, vol. 18, no. 6, pp. 1024–1032, 2021 (cit. on p. 2).
- [8] M. D. Bogaard, P. A. Doevendans, G. E. Leenders, P. Loh, R. N. Hauer, H. van Wessel, and M. Meine, “Can optimization of pacing settings compensate for a non-optimal left ventricular pacing site?” *EP Europace*, vol. 12, no. 9, pp. 1262–1269, Jun. 2010 (cit. on p. 2).
- [9] W. M. van Everdingen, M. J. Cramer, P. A. Doevendans, and M. Meine, “Quadripolar leads in cardiac resynchronization therapy,” *JACC: Clinical Electrophysiology*, vol. 1, no. 4, pp. 225–237, 2015 (cit. on p. 2).
- [10] J. P. Singh, H. U. Klein, D. T. Huang, S. Reek, M. Kuniss, A. Quesada, A. Barsheshet, D. Cannom, I. Goldenberg, S. McNitt, J. P. Daubert, W. Zareba, and A. J. Moss, “Left ventricular lead position and clinical outcome in the multicenter automatic defibrillator implantation trial-cardiac resynchronization therapy (MADIT-CRT) trial,” *Circulation*, vol. 123, no. 11, pp. 1159–1166, 2011 (cit. on p. 2).
- [11] M. Svendsen, F. W. Prinzen, M. K. Das, Z. Berwick, M. Rybka, J. D. Tune, W. Combs, E. J. Berbari, and G. S. Kassab, “Bi-ventricular pacing improves pump function only with adequate myocardial perfusion in canine hearts with pseudo-left bundle branch block,” *Experimental Biology and Medicine*, vol. 237, no. 6, pp. 644–651, 2012 (cit. on p. 2).
- [12] L. A. Saxon, B. Olshansky, K. Volosin, J. S. Steinberg, B. K. Lee, G. Tomassoni, T. Guarnieri, A. Rao, P. Yong, E. Galle, J. Leigh, F. Ecklund, and M. R. Bristow, “Influence of left ventricular lead location on outcomes in the COMPANION study,” *Journal of Cardiovascular Electrophysiology*, vol. 20, no. 7, pp. 764–768, 2009 (cit. on p. 2).

- [13] R. H. Helm, M. Byrne, P. A. Helm, S. K. Daya, N. F. Osman, R. Tunin, H. R. Halperin, R. D. Berger, D. A. Kass, and A. C. Lardo, “Three-dimensional mapping of optimal left ventricular pacing site for cardiac resynchronization,” *Circulation*, vol. 115, no. 8, pp. 953–961, 2007 (cit. on p. 2).
- [14] C. Butter, A. Auricchio, C. Stellbrink, M. Schlegl, E. Fleck, W. Hörsch, E. Huvelle, J. Ding, and A. Kramer, “Should stimulation site be tailored in the individual heart failure patient?” *American Journal of Cardiology*, vol. 86, no. 9, K144–K151, 2000 (cit. on p. 2).
- [15] L. Fan, J. S. Choy, F. Raissi, G. S. Kassab, and L. C. Lee, “Optimization of cardiac resynchronization therapy based on a cardiac electromechanics-perfusion computational model,” *Computers in Biology and Medicine*, vol. 141, p. 105 050, 2022 (cit. on pp. 2, 5).
- [16] A. Craine, A. Krishnamurthy, C. T. Villongco, K. Vincent, D. E. Krummen, S. M. Narayan, R. C. P. Kerckhoffs, J. H. Omens, F. Contijoch, and A. D. McCulloch, “Successful cardiac resynchronization therapy reduces negative septal work in patient-specific models of dyssynchronous heart failure,” *PLOS Computational Biology*, vol. 20, no. 10, pp. 1–23, Oct. 2024 (cit. on p. 2).
- [17] R. C. Kerckhoffs, A. D. McCulloch, J. H. Omens, and L. J. Mulligan, “Effects of biventricular pacing and scar size in a computational model of the failing heart with left bundle branch block,” *Medical Image Analysis*, vol. 13, no. 2, pp. 362–369, 2009, Includes Special Section on Functional Imaging and Modelling of the Heart (cit. on p. 2).
- [18] M. Albatat, H. Arevalo, J. Bergsland, V. Strøm, I. Balasingham, and H. H. Odland, “Optimal pacing sites in cardiac resynchronization by left ventricular activation front analysis,” *Computers in Biology and Medicine*, vol. 128, p. 104 159, 2021 (cit. on p. 2).
- [19] E. F. Carpio, J. F. Gomez, R. Sebastian, A. Lopez-Perez, E. Castellanos, J. Almendral, J. M. Ferrero, and B. Trenor, “Optimization of lead placement in the right ventricle during cardiac resynchronization therapy. a simulation study,” *Frontiers in Physiology*, vol. 10, 2019 (cit. on p. 2).
- [20] A. W. C. Lee, C. M. Costa, M. Strocchi, C. A. Rinaldi, and S. A. Niederer, “Computational modeling for cardiac resynchronization therapy,” *Journal of Cardiovascular Translational Research*, vol. 11, no. 2, pp. 92–108, 2018 (cit. on p. 2).
- [21] C. T. Villongco, D. E. Krummen, J. H. Omens, and A. D. McCulloch, “Non-invasive, model-based measures of ventricular electrical dyssynchrony for predicting CRT outcomes,” *EP Europace*, vol. 18, no. Suppl 4, pp. iv104–iv112, Dec. 2016 (cit. on p. 2).
- [22] M. Pluijmert, P. Bovendeerd, J. Lumens, K. Vernooy, F. W. Prinzen, and T. Delhaas, “New insights from a computational model on the relation between pacing site and CRT response,” *EP Europace*, vol. 18, no. Suppl 4, pp. iv94–iv103, Dec. 2016 (cit. on p. 2).
- [23] P. R. Huntjens, J. Walmsley, S. Ploux, P. Bordachar, F. W. Prinzen, T. Delhaas, and J. Lumens, “Influence of left ventricular lead position relative to scar location on response to cardiac resynchronization therapy: A model study,” *EP Europace*, vol. 16, no. Suppl 4, pp. iv62–iv68, Nov. 2014 (cit. on p. 2).
- [24] S. A. Niederer, A. K. Shetty, G. Plank, J. Bostock, R. Razavi, N. P. Smith, and C. A. Rinaldi, “Biophysical modeling to simulate the response to multisite left ventricular stimulation using a quadripolar pacing lead,” *Pacing and Clinical Electrophysiology*, vol. 35, no. 2, pp. 204–214, 2012 (cit. on p. 2).
- [25] J. Constantino, Y. Hu, and N. A. Trayanova, “A computational approach to understanding the cardiac electromechanical activation sequence in the normal and failing heart, with translation to the clinical practice of CRT,” *Progress in Biophysics and Molecular Biology*, vol. 110, no. 2, pp. 372–379, 2012, SI: Beating Heart (cit. on p. 2).

- [26] E. Naghavi, H. Wang, L. Fan, J. S. Choy, G. Kassab, S. Baek, and L.-C. Lee, “Rapid estimation of left ventricular contractility with a physics-informed neural network inverse modeling approach,” *Artificial Intelligence in Medicine*, vol. 157, p. 102 995, 2024 (cit. on p. 2).
- [27] Y. Dabiri, A. Van der Velden, K. L. Sack, J. S. Choy, G. S. Kassab, and J. M. Guccione, “Prediction of left ventricular mechanics using machine learning,” *Frontiers in Physics*, vol. 7, 2019 (cit. on p. 2).
- [28] M. Alber, A. Buganza Tepole, W. R. Cannon, S. De, S. Dura-Bernal, K. Garikipati, G. Karniadakis, W. W. Lytton, P. Perdikaris, L. Petzold, and E. Kuhl, “Integrating machine learning and multiscale modeling—perspectives, challenges, and opportunities in the biological, biomedical, and behavioral sciences,” *npj Digital Medicine*, vol. 2, no. 1, Dec. 2019 (cit. on p. 2).
- [29] G. Maher, N. Wilson, and A. Marsden, “Accelerating cardiovascular model building with convolutional neural networks,” *Medical & Biological Engineering & Computing*, vol. 57, no. 10, pp. 2319–2335, 2019, Epub 2019 Aug 24 (cit. on p. 2).
- [30] M. Sacks, S. Motiwale, C. Goodbrake, and W. Zhang, “Neural network approaches for soft biological tissue and organ simulations,” *Journal of Biomechanical Engineering*, vol. 144, Sep. 2022 (cit. on p. 2).
- [31] C. Ruiz Herrera, T. Grandits, G. Plank, P. Perdikaris, F. Sahli Costabal, and S. Pezzuto, “Physics-informed neural networks to learn cardiac fiber orientation from multiple electroanatomical maps,” *Engineering with Computers*, vol. 38, no. 5, pp. 3957–3973, 2022 (cit. on p. 2).
- [32] S. Buoso, T. Joyce, and S. Kozerke, “Personalising left-ventricular biophysical models of the heart using parametric physics-informed neural networks,” *Medical Image Analysis*, vol. 71, p. 102 066, 2021 (cit. on pp. 2, 3, 11, 18).
- [33] F. Kong, N. Wilson, and S. Shadden, “A deep-learning approach for direct whole-heart mesh reconstruction,” *Medical Image Analysis*, vol. 74, p. 102 222, 2021 (cit. on p. 2).
- [34] G. C. Y. Peng, M. Alber, A. B. Tepole, W. R. Cannon, S. De, S. Dura-Bernal, K. Garikipati, G. Karniadakis, W. W. Lytton, P. Perdikaris, L. Petzold, and E. Kuhl, “Multiscale modeling meets machine learning: What can we learn?” *Archives of Computational Methods in Engineering*, vol. 28, no. 3, pp. 1017–1037, 2021 (cit. on p. 2).
- [35] A. Rasheed, O. San, and T. Kvamsdal, “Digital twin: Values, challenges and enablers from a modeling perspective,” *IEEE Access*, vol. 8, pp. 21 980–22 012, 2020 (cit. on p. 2).
- [36] Y. Dabiri, A. Van der Velden, K. L. Sack, *et al.*, “Application of feed forward and recurrent neural networks in simulation of left ventricular mechanics,” *Scientific Reports*, vol. 10, p. 22 298, 2020 (cit. on p. 2).
- [37] F. Sahli Costabal, Y. Yang, P. Perdikaris, D. E. Hurtado, and E. Kuhl, “Physics-informed neural networks for cardiac activation mapping,” *Frontiers in Physics*, vol. 8, 2020 (cit. on p. 2).
- [38] Y.-F. Chang, K.-C. Yen, C.-L. Wang, S.-Y. Chen, J. Chen, P.-H. Chu, and C.-S. Lai, “Deep learning significantly boosts CRT response prediction using synthetic longitudinal strain data: Training on synthetic data and testing on real patients,” *Biomedical Journal*, p. 100 803, 2024 (cit. on p. 2).
- [39] B. E. Odigwe, A. B. Rajeeoni, C. I. Odigwe, F. G. Spinale, and H. Valafar, “Application of machine learning for patient response prediction to cardiac resynchronization therapy,” in *Proceedings of the 13th ACM International Conference on Bioinformatics, Computa-*

- tional Biology and Health Informatics*, ser. BCB '22, New York, NY, USA: Association for Computing Machinery, 2022 (cit. on p. 2).
- [40] P. C. Wouters, R. R. van de Leur, M. B. Vessies, A. M. W. van Stipdonk, M. A. Ghossein, R. J. Hassink, P. A. Doevendans, P. van der Harst, A. H. Maass, F. W. Prinzen, K. Vernooy, M. Meine, and R. van Es, “Electrocardiogram-based deep learning improves outcome prediction following cardiac resynchronization therapy,” *European Heart Journal*, vol. 44, no. 8, pp. 680–692, Nov. 2022 (cit. on p. 2).
- [41] M. Tokodi, W. R. Schwertner, A. Kovács, Z. Tösér, L. Staub, A. Sárkány, B. K. Lakatos, A. Behon, A. M. Boros, P. Perge, V. Kutyifa, G. Széplaki, L. Gellér, B. Merkely, and A. Kosztin, “Machine learning-based mortality prediction of patients undergoing cardiac resynchronization therapy: The SEMMELWEIS-CRT score,” *European Heart Journal*, vol. 41, no. 18, pp. 1747–1756, Jan. 2020 (cit. on p. 2).
- [42] A. K. Feeny, J. Rickard, D. Patel, S. Toro, K. M. Trulock, C. J. Park, M. A. LaBarbera, N. Varma, M. J. Niebauer, S. Sinha, E. Z. Gorodeski, R. A. Grimm, X. Ji, J. Barnard, A. Madabhushi, *et al.*, “Machine learning prediction of response to cardiac resynchronization therapy,” *Circulation: Arrhythmia and Electrophysiology*, vol. 12, no. 7, e007316, 2019 (cit. on p. 2).
- [43] M. M. Kalscheur, R. T. Kipp, M. C. Tattersall, C. Mei, K. A. Buhr, D. L. DeMets, M. E. Field, L. L. Eckhardt, and C. D. Page, “Machine learning algorithm predicts cardiac resynchronization therapy outcomes,” *Circulation: Arrhythmia and Electrophysiology*, vol. 11, no. 1, e005499, 2018 (cit. on p. 2).
- [44] S. Fresca, A. Manzoni, L. Dedè, and A. Quarteroni, “Deep learning-based reduced order models in cardiac electrophysiology,” *PLOS ONE*, vol. 15, no. 10, pp. 1–32, Oct. 2020 (cit. on p. 2).
- [45] F. Regazzoni, M. Salvador, L. Dede’, and A. Quarteroni, “A machine learning method for real-time numerical simulations of cardiac electromechanics,” *Computer Methods in Applied Mechanics and Engineering*, vol. 393, p. 114 825, 2022 (cit. on p. 2).
- [46] S. Giffard-Roisin, H. Delingette, T. Jackson, J. Webb, L. Fovargue, J. Lee, C. A. Rinaldi, R. Razavi, N. Ayache, and M. Sermesant, “Transfer learning from simulations on a reference anatomy for ECGI in personalized cardiac resynchronization therapy,” *IEEE Transactions on Biomedical Engineering*, vol. 66, no. 2, pp. 343–353, 2019 (cit. on p. 2).
- [47] S. Fresca, A. Manzoni, L. Dedè, and A. Quarteroni, “POD-enhanced deep learning-based reduced order models for the real-time simulation of cardiac electrophysiology in the left atrium,” *Frontiers in Physiology*, vol. Volume 12 - 2021, 2021 (cit. on p. 2).
- [48] S. Pagani and A. Manzoni, “Enabling forward uncertainty quantification and sensitivity analysis in cardiac electrophysiology by reduced order modeling and machine learning,” *International Journal for Numerical Methods in Biomedical Engineering*, vol. 37, no. 6, e3450, 2021 (cit. on p. 2).
- [49] A. Sanchez-Gonzalez, J. Godwin, T. Pfaff, R. Ying, J. Leskovec, and P. W. Battaglia, “Learning to simulate complex physics with graph networks,” in *Proceedings of the 37th International Conference on Machine Learning*, ser. ICML’20, JMLR.org, 2020 (cit. on p. 2).
- [50] X. Morales, J. Mill, G. Simeon, K. A. Juhl, O. De Backer, R. R. Paulsen, and O. Camara, “Geometric deep learning for the assessment of thrombosis risk in the left atrial appendage,” in *Functional Imaging and Modeling of the Heart*, D. B. Ennis, L. E. Perotti, and V. Y. Wang, Eds., Cham: Springer International Publishing, 2021, pp. 639–649 (cit. on p. 2).

- [51] A. Kazemi, I. J. Abecassis, and A. A. Amini, “Pi-gnn: Physics-informed graph neural network for super-resolution of 4D flow MRI,” in *2024 IEEE International Symposium on Biomedical Imaging (ISBI)*, 2024, pp. 1–5 (cit. on p. 2).
- [52] M. Ivantsits, L. Tautz, M. Huellebrand, L. Walczak, S. Akansel, I. Khasyanova, J. Kempfert, S. Sündermann, V. Falk, and A. Hennemuth, “MV-GNN: Generation of continuous geometric representations of mitral valve motion from 3D+t echocardiography,” *Computers in Biology and Medicine*, vol. 182, p. 109 154, 2024 (cit. on p. 2).
- [53] D. Dalton, D. Husmeier, and H. Gao, “Physics-informed graph neural network emulation of soft-tissue mechanics,” *Computer Methods in Applied Mechanics and Engineering*, vol. 417, p. 116 351, 2023 (cit. on p. 2).
- [54] L. Pegolotti, M. R. Pfaller, N. L. Rubio, K. Ding, R. Brugarolas Brufau, E. Darve, and A. L. Marsden, “Learning reduced-order models for cardiovascular simulations with graph neural networks,” *Computers in Biology and Medicine*, vol. 168, p. 107 676, 2024 (cit. on p. 2).
- [55] N. Kovachki, Z. Li, B. Liu, K. Azizzadenesheli, K. Bhattacharya, A. Stuart, and A. Anandkumar, “Neural operator: Learning maps between function spaces with applications to PDEs,” *Journal of Machine Learning Research*, vol. 24, no. 89, pp. 1–97, 2023 (cit. on pp. 2, 10).
- [56] K. Azizzadenesheli, N. Kovachki, Z. Li, M. Liu-Schiaffini, J. Kossaifi, and A. Anandkumar, “Neural operators for accelerating scientific simulations and design,” *Nature Reviews Physics*, vol. 6, no. 5, pp. 320–328, 2024 (cit. on p. 2).
- [57] M. Yin, N. Charon, R. Brody, L. Lu, N. Trayanova, and M. Maggioni, “A scalable framework for learning the geometry-dependent solution operators of partial differential equations,” *Nature Computational Science*, vol. 4, no. 12, pp. 928–940, 2024 (cit. on pp. 2, 18).
- [58] H. Gao and S. Ji, “Graph U-Nets,” *IEEE Transactions on Pattern Analysis and Machine Intelligence*, vol. 44, no. 9, pp. 4948–4960, 2022 (cit. on pp. 2, 6).
- [59] Z. Li, N. B. Kovachki, C. Choy, B. Li, J. Kossaifi, S. P. Otta, M. A. Nabian, M. Stadler, C. Hundt, K. Azizzadenesheli, and A. Anandkumar, “Geometry-informed neural operator for large-scale 3D PDEs,” in *Thirty-seventh Conference on Neural Information Processing Systems*, 2023 (cit. on pp. 2, 7, 9, 18).
- [60] M. M. Bronstein, J. Bruna, T. Cohen, and P. Veličković, *Geometric deep learning: Grids, groups, graphs, geodesics, and gauges*, 2021 (cit. on p. 2).
- [61] J. D. Bayer, R. C. Blake, G. Plank, and N. A. Trayanova, “A novel rule-based algorithm for assigning myocardial fiber orientation to computational heart models,” *Annals of Biomedical Engineering*, vol. 40, no. 10, pp. 2243–2254, 2012 (cit. on pp. 3, 5).
- [62] R. R. Aliev and A. V. Panfilov, “A simple two-variable model of cardiac excitation,” *Chaos, Solitons & Fractals*, vol. 7, no. 3, pp. 293–301, 1996 (cit. on pp. 3–5).
- [63] M. Lorange and R. M. Gulrajani, “A computer heart model incorporating anisotropic propagation: I. model construction and simulation of normal activation,” *Journal of Electrocardiology*, vol. 26, no. 4, pp. 245–261, 1993 (cit. on p. 5).
- [64] R. Plonsey and R. Barr, “Current flow patterns in two-dimensional anisotropic bisyncytia with normal and extreme conductivities,” *Biophysical Journal*, vol. 45, no. 3, pp. 557–571, 1984 (cit. on p. 5).

- [65] E. Surkova, L. P. Badano, R. Bellu, P. Aruta, F. Sambugaro, G. Romeo, F. Migliore, and D. Muraru, “Left bundle branch block: From cardiac mechanics to clinical and diagnostic challenges,” *EP Europace*, vol. 19, no. 8, pp. 1251–1271, Apr. 2017 (cit. on p. 5).
- [66] J. Arumugam, J. Mojumder, G. Kassab, and L. C. Lee, “Model of anisotropic reverse cardiac growth in mechanical dyssynchrony,” *Scientific Reports*, vol. 9, no. 1, p. 12670, 2019 (cit. on p. 5).
- [67] F. Brezzi, J. Douglas, and L. D. Marini, “Two families of mixed finite elements for second order elliptic problems,” *Numerische Mathematik*, vol. 47, 217–235, 1985 (cit. on p. 5).
- [68] M. S. Alnaes, J. Blechta, J. Hake, A. Johansson, B. Kehlet, A. Logg, C. N. Richardson, J. Ring, M. E. Rognes, and G. N. Wells, “The FEniCS project version 1.5,” *Archive of Numerical Software*, vol. 3, 2015 (cit. on p. 5).
- [69] A. Logg, K.-A. Mardal, G. N. Wells, *et al.*, *Automated Solution of Differential Equations by the Finite Element Method*. Springer, 2012 (cit. on p. 5).
- [70] A. Logg and G. N. Wells, “DOLFIN: automated finite element computing,” *ACM Transactions on Mathematical Software*, vol. 37, 2010 (cit. on p. 5).
- [71] O. Ronneberger, P. Fischer, and T. Brox, “U-Net: Convolutional networks for biomedical image segmentation,” in *Medical Image Computing and Computer-Assisted Intervention – MICCAI 2015*, Cham: Springer International Publishing, 2015, pp. 234–241 (cit. on p. 6).
- [72] F. Bonnet, J. A. Mazari, T. Munzer, P. Yser, and patrick gallinari, “An extensible benchmarking Graph-Mesh dataset for studying steady-state incompressible navier-stokes equations,” in *ICLR 2022 Workshop on Geometrical and Topological Representation Learning*, 2022 (cit. on p. 6).
- [73] W. L. Hamilton, R. Ying, and J. Leskovec, “Inductive representation learning on large graphs,” in *Proceedings of the 31st International Conference on Neural Information Processing Systems*, ser. NIPS’17, Long Beach, California, USA: Curran Associates Inc., 2017, pp. 1025–1035 (cit. on p. 6).
- [74] A. Anandkumar, K. Azizzadenesheli, K. Bhattacharya, N. Kovachki, Z. Li, B. Liu, and A. Stuart, “Neural operator: Graph kernel network for partial differential equations,” in *ICLR 2020 Workshop on Integration of Deep Neural Models and Differential Equations*, 2019 (cit. on p. 8).
- [75] J. Gilmer, S. S. Schoenholz, P. F. Riley, O. Vinyals, and G. E. Dahl, “Neural message passing for quantum chemistry,” in *International conference on machine learning*, PMLR, 2017, pp. 1263–1272 (cit. on p. 8).
- [76] Z. Li, N. B. Kovachki, K. Azizzadenesheli, B. liu, K. Bhattacharya, A. Stuart, and A. Anandkumar, “Fourier neural operator for parametric partial differential equations,” in *International Conference on Learning Representations*, 2021 (cit. on p. 9).
- [77] J. W. Cooley and J. W. Tukey, “An algorithm for the machine calculation of complex Fourier series,” *Mathematics of Computation*, vol. 19, no. 90, pp. 297–301, 1965 (cit. on p. 9).
- [78] Z. Li, N. Kovachki, K. Azizzadenesheli, B. Liu, K. Bhattacharya, A. Stuart, and A. Anandkumar, “Multipole graph neural operator for parametric partial differential equations,” in *Proceedings of the 34th International Conference on Neural Information Processing Systems*, ser. NIPS ’20, Vancouver, BC, Canada: Curran Associates Inc., 2020 (cit. on p. 9).

- [79] J. Ansel, E. Yang, H. He, N. Gimelshein, A. Jain, M. Voznesensky, B. Bao, P. Bell, D. Berard, E. Burovski, G. Chauhan, A. Chourdia, W. Constable, A. Desmaison, Z. DeVito, *et al.*, “PyTorch 2: Faster machine learning through dynamic python bytecode transformation and graph compilation,” in *Proceedings of the 29th ACM International Conference on Architectural Support for Programming Languages and Operating Systems, Volume 2*, ser. ASPLOS ’24, La Jolla, CA, USA: Association for Computing Machinery, 2024, pp. 929–947 (cit. on p. 10).
- [80] M. Fey and J. E. Lenssen, “Fast graph representation learning with PyTorch Geometric,” in *ICLR Workshop on Representation Learning on Graphs and Manifolds*, 2019 (cit. on p. 10).
- [81] J. Kossaiji, N. Kovachki, Z. Li, D. Pitt, M. Liu-Schiaffini, R. J. George, B. Bonev, K. Azizzadenesheli, J. Berner, and A. Anandkumar, *A library for learning neural operators*, 2024 (cit. on p. 10).
- [82] I. Loshchilov and F. Hutter, “Decoupled weight decay regularization,” in *International Conference on Learning Representations*, 2019 (cit. on p. 10).
- [83] J. Wilczek, T. Jadczyk, W. Wojakowski, and K. S. Gołba, “Time-related factors predicting a positive response to cardiac resynchronisation therapy in patients with heart failure,” *Scientific Reports*, vol. 13, no. 1, p. 8524, 2023 (cit. on p. 10).
- [84] M. Villegas-Martinez, H. H. Odland, L.-E. Hammersbøen, O. J. Sletten, M. Stugaard, M. Witsø, F. Khan, A. Wajdan, O. J. Elle, and E. W. Remme, “Pulse arrival time variation as a non-invasive marker of acute response to cardiac resynchronization therapy,” *EP Europace*, vol. 25, no. 3, pp. 1183–1192, Feb. 2023 (cit. on p. 10).
- [85] M. O. Sweeney, R. J. van Bommel, M. J. Schalijs, C. J. W. Borleffs, A. S. Hellkamp, and J. J. Bax, “Analysis of ventricular activation using surface electrocardiography to predict left ventricular reverse volumetric remodeling during cardiac resynchronization therapy,” *Circulation*, vol. 121, no. 5, pp. 626–634, 2010 (cit. on p. 10).
- [86] R. Storn and K. Price, “Differential evolution - a simple and efficient heuristic for global optimization over continuous spaces,” *Journal of Global Optimization*, vol. 11, pp. 341–359, Jan. 1997 (cit. on p. 11).
- [87] K. Price, R. M. Storn, and J. A. Lampinen, *Differential Evolution: A Practical Approach to Global Optimization (Natural Computing Series)*. Berlin, Heidelberg: Springer-Verlag, 2005 (cit. on p. 11).
- [88] P. Virtanen, R. Gommers, T. E. Oliphant, M. Haberland, T. Reddy, D. Cournapeau, E. Burovski, P. Peterson, W. Weckesser, J. Bright, S. J. van der Walt, M. Brett, J. Wilson, K. J. Millman, N. Mayorov, *et al.*, “SciPy 1.0: Fundamental Algorithms for Scientific Computing in Python,” *Nature Methods*, vol. 17, pp. 261–272, 2020 (cit. on p. 11).
- [89] N. Toussaint, C. T. Stoeck, T. Schaeffter, S. Kozerke, M. Sermesant, and P. G. Batchelor, “In vivo human cardiac fibre architecture estimation using shape-based diffusion tensor processing,” *Medical Image Analysis*, vol. 17, no. 8, pp. 1243–1255, 2013 (cit. on p. 11).
- [90] W. Ju, S. Yi, Y. Wang, Z. Xiao, Z. Mao, H. Li, Y. Gu, Y. Qin, N. Yin, S. Wang, X. Liu, X. Luo, P. S. Yu, and M. Zhang, *A survey of graph neural networks in real world: Imbalance, noise, privacy and OOD challenges*, 2024 (cit. on p. 17).
- [91] T. Chen, K. Zhou, K. Duan, W. Zheng, P. Wang, X. Hu, and Z. Wang, “Bag of tricks for training deeper graph neural networks: A comprehensive benchmark study,” *IEEE Transactions on Pattern Analysis and Machine Intelligence*, vol. 45, no. 3, pp. 2769–2781, 2023 (cit. on p. 17).

- [92] G. Li, M. Müller, G. Qian, I. C. Delgadillo, A. Abualshour, A. Thabet, and B. Ghanem, “DeepGCNs: Making GCNs go as deep as CNNs,” *IEEE Transactions on Pattern Analysis and Machine Intelligence*, vol. 45, no. 6, pp. 6923–6939, 2023 (cit. on p. 17).
- [93] P. Wang, W. Zheng, T. Chen, and Z. Wang, “Anti-oversmoothing in deep vision transformers via the Fourier domain analysis: From theory to practice,” in *International Conference on Learning Representations*, 2022 (cit. on p. 17).
- [94] K. Oono and T. Suzuki, “Graph neural networks exponentially lose expressive power for node classification,” in *International Conference on Learning Representations*, 2020 (cit. on p. 17).
- [95] U. Alon and E. Yahav, “On the bottleneck of graph neural networks and its practical implications,” in *International Conference on Learning Representations*, 2021 (cit. on p. 17).
- [96] H. Wu, H. Luo, H. Wang, J. Wang, and M. Long, “Transolver: A fast transformer solver for PDEs on general geometries,” in *Proceedings of the 41st International Conference on Machine Learning*, ser. ICML’24, Vienna, Austria: JMLR.org, 2024 (cit. on p. 18).
- [97] M. Elrefaie, A. Dai, and F. Ahmed, “DrivAerNet: A parametric car dataset for data-driven aerodynamic design and graph-based drag prediction,” in *Volume 3A: 50th Design Automation Conference (DAC), International Design Engineering Technical Conferences and Computers and Information in Engineering Conference*, Aug. 2024, V03AT03A019 (cit. on p. 18).
- [98] M. Raissi, P. Perdikaris, and G. Karniadakis, “Physics-informed neural networks: A deep learning framework for solving forward and inverse problems involving nonlinear partial differential equations,” *Journal of Computational Physics*, vol. 378, pp. 686–707, 2019 (cit. on p. 19).
- [99] Z. Li, H. Zheng, N. Kovachki, D. Jin, H. Chen, B. Liu, K. Azizzadenesheli, and A. Anandkumar, “Physics-informed neural operator for learning partial differential equations,” *ACM / IMS J. Data Sci.*, vol. 1, no. 3, pp. 1–27, May 2024 (cit. on p. 19).
- [100] S. Goswami, A. Bora, Y. Yu, and G. E. Karniadakis, “Physics-informed deep neural operator networks,” in *Machine Learning in Modeling and Simulation: Methods and Applications*. Cham: Springer International Publishing, 2023, pp. 219–254 (cit. on p. 19).